Precise determinations of ionization potentials and *EF*-state energy levels of H_2, HD, and D_2

J. M. Gilligan*
Physics Department, Yale University, New Haven, Connecticut 06511

E. E. Eyler
Department of Physics and Astronomy, University of Delaware, Newark, Delaware 19716
(Received 20 January 1992)

We report measurements of excited states in the three stable isotopic variants of molecular hydrogen: H_2, D_2, and HD. The lowest rovibrational levels of the $EF\,^1\Sigma_g^+$ state have been measured by Doppler-free two-photon laser spectroscopy for all three molecules. The accuracy is 0.015 cm^{-1}, and will improve to 0.003 cm^{-1} when wavelength calibrations of I_2 reference transitions are completed. We also describe accurate measurements of high Rydberg *np* states in HD, and their analysis using multichannel quantum-defect theory. For HD these measurements give a result of 124 568.479(20) cm^{-1} for the ionization potential, in excellent agreement with theory. For H_2, the measurements of *EF*-state transitions give results slightly lower than previous experimental values, but the ionization potential remains in good agreement with theory. For D_2 the results reported here, when taken in combination with recent measurements of transitions between excited states by Jungen *et al.* [J. Mol. Spectrosc. (to be published)], yield a value for the ionization potential that is again quite close to the theoretical result.

PACS number(s): 35.20.Vf, 33.80.Rv, 33.20.Ni

I. INTRODUCTION

The ionization potential (IP) of molecular hydrogen has recently been measured with an accuracy of 0.015 cm^{-1} [1–3], and the best *ab initio* calculations have attained comparable accuracy [4–8]. The experimental uncertainty is about 5% of the size of the radiative corrections, providing an opportunity for a highly demanding test of fundamental molecular physics. Remarkably, the current experimental and theoretical results agree within 0.01 cm^{-1} for H_2. However, a similar comparison has not been possible for D_2 and HD because the experimental results have languished at a far less precise standard. Even for H_2 the accuracy obtained in Ref. [1] is limited less by fundamental constraints than by comparatively minor problems with wavelength metrology. In this paper we report new measurements of the IP of HD. In addition we have made highly accurate measurements of the lowest *EF*-state energy levels in all three stable isotopic variants. The results for H_2 and D_2, when used in conjunction with other recent and planned experiments, can yield significantly improved IP values for these species as well.

Recent experimental progress in measurements of the IP is summarized in Refs. [2] and [9]. Advances in accuracy have been quite rapid for H_2, with an overall improvement by a factor of about 30 since 1972. Much of this improvement stems from the introduction of laser techniques involving multiphoton, multistep excitation directly from the ground state, starting with the work of Glab and Hessler [10]. Nevertheless, more conventional spectroscopic methods have continued to play a role, and one of the most recent contributions is the extensive series of infrared measurements in H_2 and D_2 undertaken by Jungen, Dabrowski, Herzberg, and Vervloet [2,3]. This *tour de force* of Fourier-transform spectroscopy determines a link between the *EF* state and the IP for both H_2 and D_2 by establishing an extensive chain of transitions terminating in high-*l* Rydberg states whose binding energies can be determined very accurately. The other recent experiments [1,10], including the HD measurements reported here, all use the basic approach shown in Fig. 1. They involve laser double resonance through the *EF* state to high Rydberg *np* states, and ex-

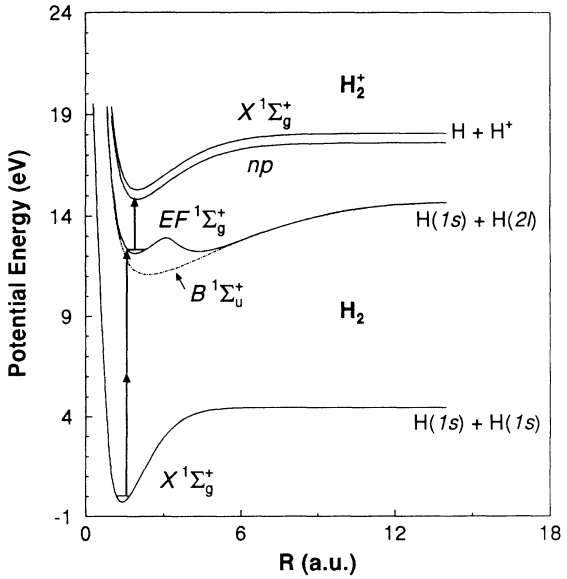

FIG. 1. Potential curves of molecular hydrogen, showing excitation scheme for multiphoton spectroscopy of $EF \leftarrow X$ and $np \leftarrow EF$ transitions.

trapolation to the limit using multichannel quantum-defect theory (MQDT). The $EF\,{}^1\Sigma_g^+$ state is a particularly well suited intermediate state for double resonance because it is one of the lowest excited states and has a fairly long lifetime of 100–200 nsec [11].

Theoretical values for the IP are obtained indirectly, by combining calculations for the dissociation energies of the neutral molecule and the molecular ion. The binding energy of atomic H is also needed, but is known both experimentally and theoretically to far higher accuracy than the 1 part in 10^7 required for present purposes. The most uncertain pieces of the theoretical puzzle appear to be the relativistic and radiative corrections.

New calculations are currently underway, the Bukowski and co-workers have very recently obtained improved results for the $H_2{}^+$ ion and its isotopic variants [6]. They obtain a value for the Bethe logarithm at the equilibrium internuclear separation that lies outside the range given by Bishop and Cheung [12–14]. However, the change to the IP itself is only about 0.001 cm^{-1}. Substantially larger changes may occur when corresponding calculations for the neutral molecules are completed. Previous calculations by Bishop and Cheung [15] relied on a moment-function interpolation method originally developed by Dalgarno and Kingston [16] and Garcia [17]. Apparently, a full calculation of radiative corrections for a two-electron, two-center system has not previously been attempted.

The two sets of measurements reported here serve different but related purposes. The first, of transitions from the $X\,{}^1\Sigma_g^+$ ground state to the $EF\,{}^1\Sigma_g^+$ excited state, provides an overall calibration of the excited-state energy spectrum relative to the ground state. The second is a determination of transition frequencies for a long sequence of Rydberg *np* states in HD; this provides a much improved value for the IP of HD. The absolute accuracy of both sets of results is presently about 0.01 cm^{-1}. However, the $EF \leftarrow X$ transitions in all three stable isotopomers have also been measured much more precisely relative to harmonics of selected hyperfine lines of I_2, using a saturated absorption cell for reference. The accuracy of the *EF*-state energy levels can be improved to 0.003 cm^{-1} simply by measuring the absolute wavelengths of these reference lines. This has very recently been accomplished by Shiner, Lichten, and Gilligan, and will be reported separately [18]. The experimental accuracy is still limited by technical considerations rather than by fundamental physical limitations, so still further improvements should be possible, eventually to the level of about 1 part in 10^9.

II. EXPERIMENT

This section describes the apparatus and techniques used for the two independent but related measurements, of $EF \leftarrow X$ transitions for H_2, D_2, and HD, and of transitions from the *EF* state to a series of singlet *np* Rydberg states in HD.

The experimental arrangement for the first set of measurements, of *EF*-state term energies, is fairly straightforward. To obtain narrow bandwidths we use Doppler-free

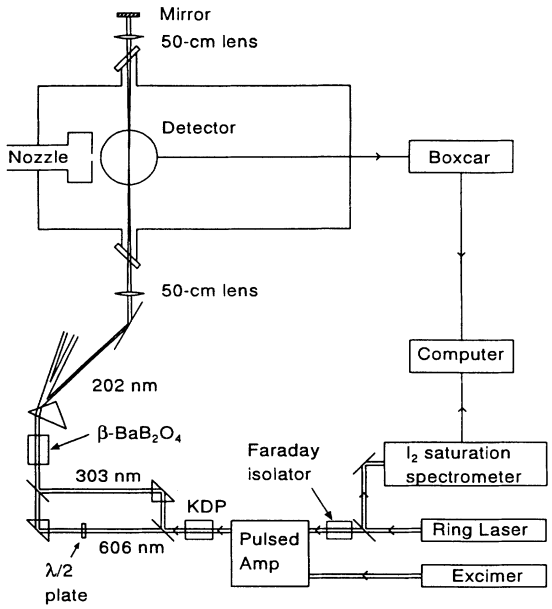

FIG. 2. Apparatus for the $EF \leftarrow X$ measurements.

two-photon excitation with counterpropagating laser beams at approximately 202 nm. This far uv laser radiation is obtained by frequently tripling the 606-nm output of a high-resolution pulse-amplified cw dye laser, as shown in Fig. 2. Transitions to the *EF* state can easily be detected by resonant multiphoton ionization, since the absorption of a third 202-nm photon ionizes the molecules to produce $H_2{}^+$, $D_2{}^+$, or HD^+ ions. The experiment is carried out in a molecular beam apparatus, using a loosely collimated supersonic expansion. The vacuum environment eliminates collisional shifts and broadening,

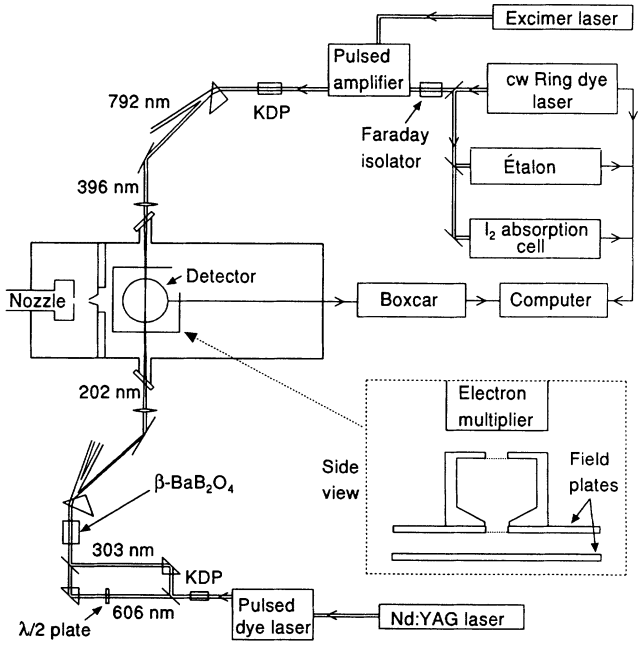

FIG. 3. Apparatus for the $np \leftarrow EF$ measurements.

and allows the use of a highly sensitive charged-particle-multiplier tube for detection.

For the second set of measurements, of $np \leftarrow EF$ transitions in HD, we use optical double resonance through the same EF-state levels. Figure 3 shows the main elements of the experimental arrangement. A low-resolution pulsed laser excites transitions to the EF state in a collimated supersonic molecular beam, then after a short delay a high-resolution laser excites $np \leftarrow EF$ transitions. The Rydberg np states are selectively detected by Stark ionization using a delayed pulsed electric field.

A. Lasers

The high-resolution laser for both experiments is a pulse-amplified cw single-mode ring dye laser. The output of a Coherent CR699-29 dye laser is amplified in an excimer-pumped three-stage amplifier (Lambda Physik FL 2003) to produce pulses of about 10-nsec duration with energies up to 14 mJ.

The narrow-band 202-nm radiation needed for two-photon $EF \leftarrow X$ transitions is produced by first frequency doubling a 606-nm laser pulse in potassium dihydrogen phosphate (KDP), then mixing the resulting second harmonic radiation with the residual fundamental beam in β-BaB_2O_4 (BBO). This technique is described in detail by Glab and Hessler [19]. Starting with 10-mJ pulses at 606 nm, pulse energies up to several hundred microjoules can be obtained at 202 nm.

To avoid possible ac Stark shifts from the intense residual 606- and 303-nm beams, the 202-nm light is separated by using both a dispersing prism and a 194-nm-high reflector, angle tuned to give maximum reflection at 202 nm.

For the double-resonance measurements of HD $np \leftarrow EF$ transitions, two tunable pulsed lasers are needed. A broadband Nd:YAG-pumped (where YAG denotes yttrium aluminum garnet) pulsed dye laser produces 606-nm light, the third harmonic of which is used to drive the $EF \leftarrow X$ "pump" step. This pump step proceeds much as in the $EF \leftarrow X$ experiment except that the laser bandwidth is about 1 cm^{-1}, and counterpropagating 202-nm beams are not used. The $np \leftarrow EF$ "probe" step is driven by narrow-band light at 395–397 nm. This light is produced by operating the cw laser and the pulsed amplifier at 790–794 nm with LDS-751 dye, then frequency doubling the output in KDP. The cavity losses in the cw laser are too large for easy operation in a ring configuration with this rather inefficient dye, so the laser was modified for standing wave operation. Chilling the laser dye with an ice-water bath substantially improves the dye efficiency and lifetime, as well as the laser stability. Nonetheless, the arrangement is so inconvenient that we plan to use a Ti:sapphire laser for future measurements. The 202- and 396-nm light beams are focused in counterpropagating directions into a molecular beam apparatus, where they intersect a collimated supersonic HD beam at right angles. As in the $EF \leftarrow X$ measurement, dispersing prisms separate the 396- and 202-nm radiation from the longer fundamental wavelengths.

B. Wavelength measurements

For both the $EF \leftarrow X$ and $np \leftarrow EF$ measurements, the cw laser wavelength is measured using the absorption spectrum of I_2. A small portion of the cw laser output is split off for metrology and divided into several beams. One beam is used for intensity normalization. A second passes through a cell of I_2 vapor. The I_2 cell is kept at room temperature for measuring the 606-nm laser used in the $EF \leftarrow X$ transitions. To obtain sufficient absorption at 792 nm for the $np \leftarrow EF$ measurements, it is necessary to heat the cell to around 800 °C, while maintaining a cold finger at room temperature to keep the I_2 vapor pressure low. A third beam passes through a 25-cm marker interferometer used to interpolate the interval between the I_2 reference line and the hydrogen transition being measured. Finally, for the EF-state measurements a fourth beam is counterpropagated through the I_2 cell, so that the Doppler-free saturated-absorption spectrum can be acquired in addition to the ordinary I_2 absorption spectrum.

The Doppler-broadened iodine absorption lines can be calibrated using the I_2 atlases of Gerstenkorn and coworkers [20–23]. For wavelengths near 600 nm the atlas has an overall uncertainty of one part in 10^7, or 0.002 cm^{-1} after correcting by -0.006 cm^{-1} for a systematic calibration error [23]. For the pump step of a total of six photons at 606 nm are used, so the resulting uncertainty in the EF-state energies is 0.012 cm^{-1}. For wavelengths near 792 nm the accuracy of the I_2 atlas degrades to around 4 parts in 10^7 or 0.005 cm^{-1} [22]. The probe step involves two photons at this wavelength. These wavelength calibration uncertainties dominate the error budget for both sets of measurements. The details of fitting the iodine lines and analyzing the resulting uncertainties are discussed in Sec. III.

To further improve the accuracy a reference spectrum with narrower linewidths is needed. Saturated absorption spectroscopy of I_2 is an obvious solution to this problem. The Doppler-broadened I_2 lines observed in ordinary absorption spectroscopy consist of 15 or 21 hyperfine components blended by their 380-MHz room-temperature Doppler widths. In saturated absorption these components are resolved as very sharp features with widths limited mainly by pressure broadening, about 3 MHz at room temperature. Unfortunately there is no comprehensive tabulation of the Doppler-free spectrum of I_2 comparable to the atlases of Gerstenkorn and coworkers [20–23], but these lines can serve as highly repeatable transfer standards. We have measured each of the $EF \leftarrow X$ transitions relative to nearby saturated-absorption lines. Very recently, Shiner, Lichten, and Gilligan have measured these I_2 reference transitions by interferometrically comparing them to a stabilized helium-neon laser [18]. As discussed below, this recalibration will immediately improve the accuracy of the $EF \leftarrow X$ measurements to 0.003 cm^{-1}.

Because of technical difficulties the $np \leftarrow EF$ transitions were recorded without saturated-absorption I_2 calibrations, but this method can be used to improve the accura-

cy of future measurements. A much lower fractional accuracy suffices for this probe step, since the pump step to the EF state at about 100 000 cm^{-1} constitutes 80% of the total transition energy from the ground state to the high Rydberg states.

When using a vapor cell as a wavelength standard, it is necessary to consider possible pressure shifts due to impurities. We filled two homemade 15-cm-long cells of fused silica using a procedure described in Ref. [24]. The cell used to calibrate the $EF \leftarrow X$ transitions was broken between the two sets of measurements, so a direct test for pressure shifts by comparing different cells is impossible. However, a reasonable upper limit for pressure shifts is set by the size of the total pressure-broadened linewidth. Saturated-absorption lines observed with this cell had widths of 6 MHz, somewhat broader than the expected 4-MHz convolution of the apparatus function with the 3-MHz collisional width of pure I_2 vapor at room temperature [25,26]. Thus we have included in our error analysis a systematic uncertainty of 6 MHz at the 606-nm fundamental wavelength.

C. Molecular beam apparatus

To provide a high density of molecular hydrogen without introducing pressure shifts, we use a supersonic expansion in a vacuum chamber. A Lasertechnics LPV pulsed nozzle produces hydrogen gas pulses with a duration of roughly 150 μsec. A movable partition divides the vacuum chamber into two differentially pumped regions. A conical skimmer can be installed in this partition to collimate the molecular beam. A small turbomolecular pump, Balzers TPH-170, is used to provide an oil-free vacuum in the laser interaction region. The pressure in this region is typically a few times 10^{-5} Torr, limited almost entirely by residual hydrogen from the molecular beam itself.

H_2 or D_2 gas is obtained from commercial cylinders with a nominal purity of 99.995% for the H_2 and 99.7% for the D_2. Since pure HD is expensive and somewhat unstable against isotopic reequilibration, we used gas from a cylinder that was filled with equal amounts of H_2 and D_2 and "aged" for several months to encourage partial equilibration of the three molecules. The concentration of HD was measured by comparing the relative sizes of $EF \leftarrow X$ transitions in HD, H_2, and D_2. The HD fraction was only about 7% after three months and about 10% after a year, but was nevertheless sufficient for usable signal sizes. The selectivity of mass-selective ion detection and double-resonance excitation eliminates any ambiguity about which isotopomer is being observed.

The $EF \leftarrow X$ measurements are performed in an uncollimated expansion since two-photon excitation with counterpropagating equal-frequency beams is intrinsically Doppler free. The 202-nm light is focused with a 50-cm lenses onto the molecular beam 4 mm from the nozzle. A second lens recollimates the light, and a uv-enhanced aluminum mirror with an Acton Research No. 2000 coating (reflectance $>90\%$) serves as a retroreflector. To reduce ac Stark shifts the lenses are backed off about 1 cm from tight focuses. We vary the laser intensity to test for residual ac Stark shifts, as described in Sec. III.

The $np \leftarrow EF$ measurements are performed in a molecular beam with a collimation ratio of 25:1, giving a residual Doppler width of 0.007 cm^{-1} for the 25 000 cm^{-1} transitions. The 396-nm probe beam is separated in time by about 80 nsec from the 202-nm pump beam, so there is no interaction between these two excitation steps. Unlike two-photon Doppler-free excitation, this arrangement leads to shifts of the line centers if the lasers are misaligned relative to the molecular beam. This misalignment is controlled within 10 mrad, corresponding to a maximum Doppler shift of 7 parts in 10^8, or 0.0017 cm^{-1} for a 25 000-cm^{-1} transition.

D. Detection

The $EF \leftarrow X$ transitions are observed by detecting H_2^+, D_2^+, or HD^+ ions with a fast multiplier tube, Thorn EMI type 143. This detector is placed 10 cm above the interaction region with its front dynode biased negatively at 2500–3000 V to collect the ions. Time-of-flight mass spectroscopy with a gated integrator distinguishes H_2^+, D_2^+, and HD^+ ions both from one another and from other ions such as H^+ or ionized hydrocarbon contaminants. Signals up to several times 10^5 ions per shot can be observed, but with signals this large the arrival time at the detector depends significantly on the signal size, presumably because of space charge or the charging of surfaces near the interaction region. The measurements are therefore conducted with attenuated 202-nm laser pulses having energies of $\lesssim 20$ μJ. The signal sizes are still as large as a few times 10^4 ions, and the variation of arrival time with signal size is eliminated.

The $np \leftarrow EF$ transitions are detected by delayed Stark ionization of the high Rydberg np states, using a pulsed electric field. The np states are extremely susceptible to dc Stark shifts from stray electric fields, so much care is required in the design of the field plates. Two brass plates 1 cm apart, coated with colloidal graphite (Acheson Colloids, Aerodag-G), shield the interaction region from electric fields. Electrons are extracted through a 1-cm hole in the top plate and detected with the same EMI electron multiplier used to detect the EF states, with its bias reversed. A wire mesh is mounted across the hole and a grounded copper drift tube is placed above it, minimizing the penetration of stray fields from the detector into the interaction region. Delayed Stark ionization is accomplished by applying a pulsed field of 300 V/cm after a delay of up to a few microseconds from the probe laser pulse. Stray photoelectrons produced directly by the pump and probe lasers are not seen, since they are produced with typical kinetic energies of 3 eV that propel them into the field plates after only a few tens of nanoseconds. We use a much longer delay before the Stark ionization pulse because this also avoids problems from transient rf noise accompanying the firing of the excimer laser.

To reduce the effect of shot-to-shot intensity variations, signal averaging is used for both sets of measurements. The signals from between three and ten succes-

sive laser shots are averaged by a boxcar averager. This process introduces an apparatus function that broadens spectral features and blue shifts them. Corrections for this shift are described in Secs. III and IV.

III. $EF \leftarrow X$ TRANSITIONS

We have measured the $Q(0)$ and $Q(1)$ branches of the $EF \leftarrow X$ transition in H_2 and HD, and the $Q(0)$, $Q(1)$, and $Q(2)$ transitions in D_2. All of these two-photon transitions are in the (0-0) vibrational band. It is also possible in principle to observe rotational O and S branches, but they are so weak that high-precision measurements are impractical.

Two sets of data were taken. One set, the "low-resolution data," was acquired by scanning over 10–20-GHz intervals relatively quickly. These data were used to measure the $EF \leftarrow X$ transitions relative to the Doppler-broadened I_2 lines. The second set of "high-resolution data" was acquired by scanning small intervals as slowly as the laser controller would allow, at 60 MHz/sec. These data were used to measure the $EF \leftarrow X$ transitions relative to the saturated-absorption spectrum of I_2. Figure 4 shows a typical high-resolution scan for D_2. The high-resolution data are five times as precise as the low-resolution data, but require a separate calibration of the reference transitions as outlined in Sec. II B.

In this section, all references to wavelength and frequency intervals refer to the full vacuum ultraviolet (VUV) transition at 101 nm, equivalent to six times the intervals at the 606-nm fundamental laser wavelength.

A. Error analysis

The major sources of uncertainty can be divided into three classes, which will be discussed in turn: (1) Errors associated with the two-photon excitation process, including ac Stark shifts and frequency shifts arising in pulsed laser amplification; (2) errors associated with data acquisition and determining the line centers of the $EF \leftarrow X$ transitions; and (3) errors associated with wavelength measurement. These include the effects of laser scan nonlinearities, which affect both sets of measurements, and uncertainties in wavelength calibration of the low-resolution data using the iodine spectrum.

To test for ac Stark shifts we measured each transition repeatedly while varying the intensity of the 202-nm beam by a factor of 3–10. We set limits on intensity-dependent shifts by looking for shifts in the hydrogen line positions relative to nearby saturated-absorption reference lines in I_2. In the worst case the limit so obtained is 45 MHz. Another estimate for ac Stark shifts can be obtained from the shift coefficient of about 3–6 MHz per MW/cm^2 reported by Hessler and Glab [27]. Our measurements were recorded with the lenses backed off 1 cm from their tight-focus positions.

Under these conditions a diffraction-limited 20-μJ pulse produces a calculated intensity at the molecular beam of about 3.2 MW/cm^2. This corresponds to an ac Stark shift of 14 MHz that can probably also be regarded as an upper limit, since the spatial mode quality of the 202-nm beam is rather poor. In our data analysis we have used the more conservative error limits from the direct intensity dependence measurements.

When a laser is pulse amplified both frequency shifts and time-dependent frequency "chirping" can be introduced. Fee, Danzmann, and Chu [28] have studied this problem. They demonstrate that the mean shift seen in an nth-order nonlinear process, such as harmonic generation or multiphoton absorption, can differ slightly from n times the shift of the fundamental laser frequency. This problem arises if the laser pulse is asymmetric in time and the frequency is appreciably chirped during the pulse. Thus it is impossible to completely correct for these effects without a measurement of the actual phase evolution of the laser pulse. However, a measurement of the average frequency shift can be used to make an approximate correction, and to determine the approximate scale

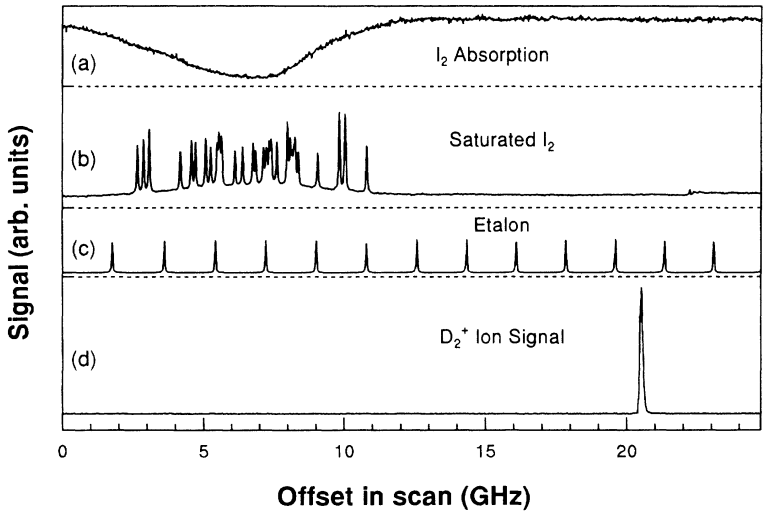

FIG. 4. Spectrum of the $Q(1)$ branch of $EF \leftarrow X$ in D_2. (a) Fully Doppler-broadened spectrum of I_2. (b) Saturated-absorption spectrum of I_2. (c) Transmission spectrum of the marker interferometer. (d) D_2^+ signal.

of possible frequency chirping within the pulse.

To measure the frequency shift we directed both the cw and pulse-amplified beams through the marker étalon and measured the positions of étalon transmission peaks relative to saturated-absorption features in I_2 observed using the cw beam. Precise alignment of the pulsed beam is difficult because the transversely pumped amplifier introduces knife-edge diffraction into the spatial mode of the laser, which we partially removed with a 2-mm iris. The measured frequency difference between the cw and pulse-amplified lasers is 5 ± 5 MHz, measured at the 606-nm fundamental wavelength. The uncertainty is limited by our ability to align both lasers properly through the étalon.

The laser frequency can be corrected for this small shift. A conservative estimate of possible additional errors from frequency chirping is made by assigning an uncertainty equal to twice the total size of the shift. Both the work of Fee, Danzmann, and Chu [28] and recent measurements by our group suggest that the pulse experiences a simple linear chirp, whose average value is the shift observed in an étalon. For this situation, the additional shifts in nonlinear processes that result from the chirp are much smaller than the average shift itself. Since this is one of the dominant uncertainties in the high-resolution $EF\leftarrow X$ measurements, it will be essential in more accurate future measurements to explicitly measure and correct for this frequency chirping. This problem is one of the fundamental limitations of laser spectroscopy in the vacuum ultraviolet region, and merits careful study.

The $EF\leftarrow X$ line centers are determined by fitting Gaussian profiles to the multiphoton ionization signals. In the high-resolution data the transitions have widths as small as 120 MHz, only twice the linewidth of about 60 MHz measured for the pulse-amplified laser at the 606-nm fundamental wavelength. Peaks in the low-resolution data are broadened noticeably by the boxcar averager. The boxcar time constant corresponds to a frequency interval of 30 MHz for the high-resolution data and 120 MHz for the low-resolution data. The effects of this time constant on the line positions have been calculated and the results corrected accordingly. This correction is accurate to 10% of the time constant or better [24].

Statistical noise in the line-center fits is negligible. However, the granularity of the data acquisition also imposes a small uncertainty, 0.0002 cm^{-1} in the high-resolution data and 0.001 cm^{-1} in the low-resolution data.

Nonlinearities in the laser scan can cause small errors in interpolating the interval between an $EF\leftarrow X$ transition and an I_2 reference line. To alleviate this problem we linearize the scans using marker fringes from a 25-cm étalon. Its free spectral range was measured to ±0.2 MHz by counting the number of fringes between two I_2 lines 2 cm^{-1} apart. It is still necessary to interpolate the small interval between a spectral feature and the nearest marker étalon fringe. This is done by cubic-spline interpolation, using the three nearest étalon fringes on each side. For a typical $EF\leftarrow X$ transition this method reduces the scatter between consecutive measurements from 17 MHz for uncorrected scans to less than 1 MHz for the interpolated scans. The uncertainty of the free spectral range of the marker étalon contributes 0.0006–0.0007 cm^{-1} to the uncertainty of the measurements. Thermal instabilities in the étalon cause additional errors as the fringes drift during a scan, introducing additional uncertainties of 0.000 06–0.0006 cm^{-1} in the low-resolution measurements and 0.000 12–0.0006 cm^{-1} in the high-resolution measurements.

The accuracy of the low-resolution measurements is limited by uncertainties associated with the Doppler-broadened I_2 reference lines. Apart from an overall uncertainty of 0.012 cm^{-1} due to the calibration of the iodine atlas, there are additional statistical uncertainties for individual lines in the atlas. These contribute 0.002–0.006 cm^{-1} to the error budget for the $EF\leftarrow X$ transitions. A further problem arises because the iodine atlas was measured using Fourier spectroscopy, with an apparatus function that slightly but noticeably broadens the lines. It has been argued that the maxima of the lines in the atlas correspond closely to the centroids of lines measured in high-resolution laser spectroscopy [23]. However, our attempts to determine the centroids of I_2 references lines failed to yield consistent results because they are quite sensitive to noise on the base line. A more repeatable method of analyzing the I_2 spectrum is to fit Gaussian line shapes to the observed lines.

Line positions determined by fitting Gaussians will agree with the atlas for symmetric lines [23]. However, problems arise because most of the I_2 lines are asymmetric due to unresolved hyperfine structure and overlapping transitions. Two methods are used to estimate the resulting errors.

In the first, the asymmetry of the individual lines is measured by comparing the results of fitting Gaussians to different portions of the line: the entire line, including a region of the base line on either side; the bulk of the line, extending almost to the base; and the central part of the line, between the two half-maximum points. The spread among these values is taken as an estimate of the error due to asymmetry, typically about 0.006 cm^{-1}.

The second method is useful only when a hydrogen transition can be referenced to two or more iodine lines. We then measure the scatter between results obtained using each reference line. Since the asymmetry of a given I_2 line is usually not related to that of other nearby lines, this gives a good measure of the quality of the wavelength calibration. This test indicates that where the lines are not grossly asymmetric to the eye, calibrations using fits to Gaussians are consistent within the uncertainties quoted in the atlas. The frequency of the hydrogen transition is then determined from the average of the iodine line calibrations, weighted by the statistical uncertainty of each I_2 line.

B. Results for $EF\leftarrow X$ transitions

Table I shows the error budget for the low-resolution measurements. The total error is taken to be the quadra-

TABLE I. Error budget for low-resolution $EF \leftarrow X$ data. Where a quantity varies between different transitions a typical value is shown. "Etalon FSR" refers to errors arising from the uncertainty in the free spectral range of the marker étalon.

I_2 atlas calibration	0.012
Uncertainties finding centers of I_2 lines	0.006
Relative uncertainties of the I_2 lines within the atlas	0.005
Errors in scan linearization	0.004
Data granularity	0.002
Laser amplifier shift	0.002 (estimated)
ac Stark shift	<0.0015
Contamination of the I_2 cell	<0.0012
Etalon FSR	0.0006
Boxcar time constant	0.0004
Etalon thermal drift	0.0004
rms Total	0.015

ture sum of the different contributions, since there is no reason to expect they are correlated. Table II shows the error budget for the high-resolution measurements, assuming the saturated-absorption I_2 reference lines are known exactly. New measurements of the saturated-absorption reference lines are accurate to a few parts in 10^{10}, so this is a reasonable assumption.

Table III gives the results of the low-resolution measurements. The two transitions in H_2 can be compared with our previous measurement of EF-state term energies, which used a very different laser configuration, and was calibrated using the spectrum of Te_2 [29]. For $N=0$, the new result is 0.022 cm^{-1} below the previous value, just within the combined error bars. To make a comparison for $N=1$, the term energy of the EF, $v=0$, $N=1$ level is calculated using the ground-state rotational interval from Ref. [30]. The new result for this level is also slightly lower, by 0.015 cm^{-1}.

Table IV gives the values for the high-resolution measurements relative to selected reference lines in the I_2 hyperfine spectrum. The values reported are the difference between the transition energy of the $EF \leftarrow X$ transition and six times the transition energy of a particular peak in the saturated-absorption spectrum of I_2. Figures 5–8 identify the features in the I_2 spectrum used as references. These results can be converted to absolute transition energies using new I_2 wavelength calibrations by Shiner, Lichten, and Gilligan, to be reported separately [18]. Preliminary results indicate that there will be no major changes to the energy levels given in Table III.

IV. *np* RYDBERG STATES

Transitions from the ($v=0$, $N=0$) level of the EF state to 38 Rydberg np states were observed, with n ranging from 40 to 80. Figure 9 shows one such transition along with metrological data. From the $N=0$ rotational level of the EF state, dipole selection rules allow only $R(0)$ rotational branches. Usable signals could not be obtained from the $N=1$ and higher levels because of inadequate rotational populations. The supersonic expansion cools the HD almost completely into the $N=0$ rotational level of the ground state, from which only $N=0$ of the EF state is accessible.

The transition frequencies were measured using the procedure outlined in Sec. III for the low-resolution $EF \leftarrow X$ data. The error budget is completely dominated by the overall calibration uncertainty of the iodine atlas in the 792-nm region, which contributes an uncertainty of 0.010 cm^{-1} to the $np \leftarrow EF$ transitions.

The np state energies follow a very erratic pattern because there is strong coupling between Rydberg series

TABLE II. Error budget for high-resolution $EF \leftarrow X$ data, showing uncertainties in the intervals between the indicated transitions and the saturated I_2 reference lines listed in Table IV. Errors due to ac Stark shifts, étalon free spectral range, and étalon instability vary from scan to scan, but contribute little to the total uncertainties.

Uncertainties finding centers in I_2 lines	0.0002
Laser amplifier shift	0.002 (estimated)
ac Stark shift	<0.0015
Contamination of the I_2 cell	<0.0012
Boxcar time const.	0.0001
Etalon FSR	<0.0007
Etalon thermal drift	<0.0008
Errors in scan linearization	0.0004
Data granularity	0.0002
Total	0.003

TABLE III. $EF \leftarrow X$ transition energies in H_2, D_2, and HD.

H_2 $Q(0)$	99 164.779(14)
H_2 $Q(1)$	99 109.727(15)
D_2 $Q(0)$	99 461.440(14)
D_2 $Q(1)$	99 433.706(15)
D_2 $Q(2)$	99 378.388(14)
HD $Q(0)$	99 301.338(17)
HD $Q(1)$	99 259.904(15)

converging to the $N^+=0$ and 2 rotational levels of the HD^+ ion. Figure 10 illustrates this situation, which is discussed in detail in Sec. V. To assign the $np \leftarrow EF$ transitions we compared the observed transition energies with predictions from a MQDT model. This model is identical to the one used in Sec. V to analyze the Rydberg series. For making initial assignments, approximate values are needed for four MQDT parameters. Calculated *ab initio* values were used for the ionization potential of HD and the $N^+=0$–2 rotational interval in HD^+. The Π-state quantum defect δ_π was taken from an analysis of Takezawa and Tanaka's measurements of $np \leftarrow X$ transitions in HD. Finally, for the Σ states we used the value of δ_σ measured for the np states of H_2 by McCormack *et al.* [1,31].

With only two exceptions the measured energies are within 0.016 cm^{-1} of the values predicted using these parameters. Since the spacing between adjacent np states ranges from 0.4 to 3.7 cm^{-1}, the assignments are completely unambiguous apart from minor problems with additional "satellite" lines, discussed below.

There was significant variation in intensity among the transitions, and the 49p and 59p states were not seen at all. Figure 11 illustrates this variation in the transitions to the 72p, 73p, and 74p states. The intensity variation is predicted in the MQDT calculations; it results from interference between the interacting Rydberg series converging to the $N^+=0$ and 2 levels of the HD^+ ion.

A number of np state transitions are accompanied by additional unidentified lines. Figure 12 shows an example of such "satellite" lines near the 60p state. When these satellite lines are present there is usually one large peak that can be identified as the p state. The amplitude of the satellites relative to the main peak generally increases with the intensity of the probe laser, but shows little dependence on the pump laser. Most of this change in relative intensities comes from saturation and depletion broadening of the main $np \leftarrow EF$ transition, which could be observed in all but the weakest transitions.

Of the 38 observed transitions, eight were accompanied by satellite lines that could not be eliminated by attenuating the probe laser. The pattern of the satellite peaks

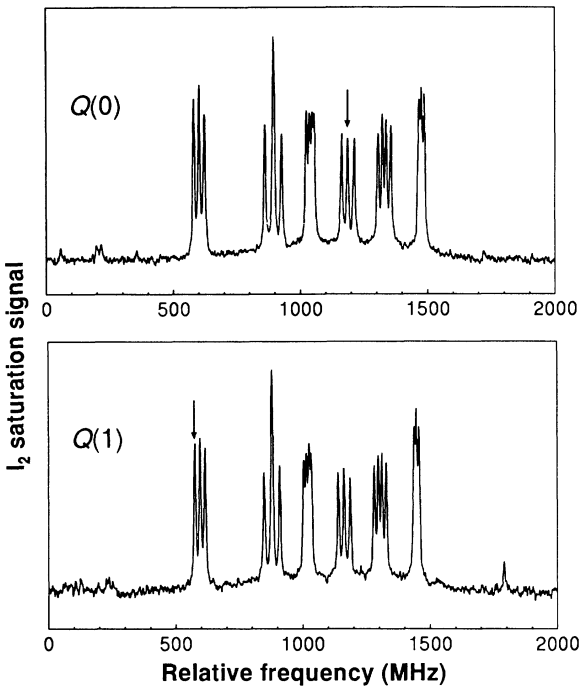

FIG. 5. Saturated I_2 lines for future calibration of $EF \leftarrow X$ in H_2. The upper figure shows the hyperfine structure of line 3286 in Ref. [20], used to calibrate the $Q(0)$ branch, and the lower figure shows line 3247, used for the $Q(1)$ branch. The arrows indicate the hyperfine components listed in Table IV.

TABLE IV. $EF \leftarrow X$ transitions relative to saturated I_2 lines. Notation follows Ref. [45].

Transition	I_2 reference line	$f_{\text{trans}} - 6f_{I_2}$ (MHz)
H_2 $Q(0)$	"i" hyperfine component of I_2 line 3286 in Ref. [20] (see Fig. 5)	31 506(80)
H_2 $Q(1)$	"o" component of I_2 line 3247 (see Fig. 5)	−19 362(80)
D_2 $Q(0)$	"s" component of I_2 line 3652 (see Fig. 6)	−450(80)
D_2 $Q(1)$	unidentified component of I_2 line 3603 (see Fig. 6)	10 074(80)
D_2 $Q(2)$	"o" component of I_2 line 3515 (see Fig. 7)	−8 520(70)
HD $Q(0)$	"i" component of I_2 line 3417 (see Fig. 8)	10 290(70)
HD $Q(1)$	unidentified component of I_2 line 3374 (see Fig. 8)	−35 412(80)

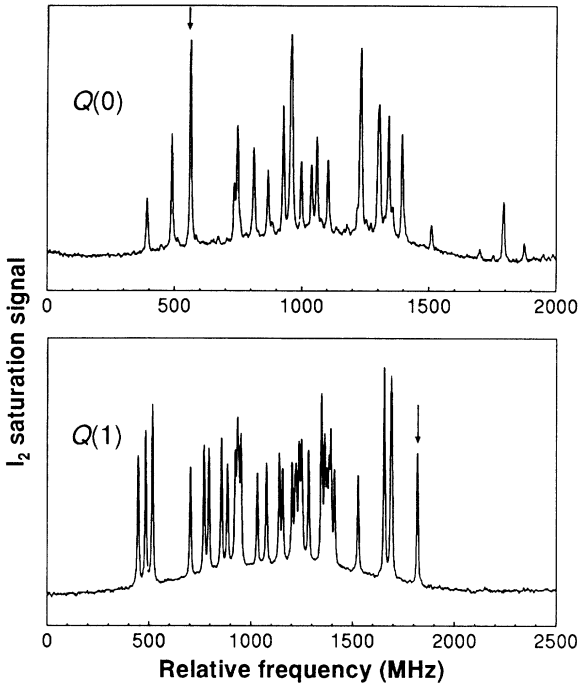

FIG. 6. Same as Fig. 5, showing I_2 line 3652, used for $Q(0)$ branch in D_2, and I_2 line 3603, used for $Q(1)$ branch.

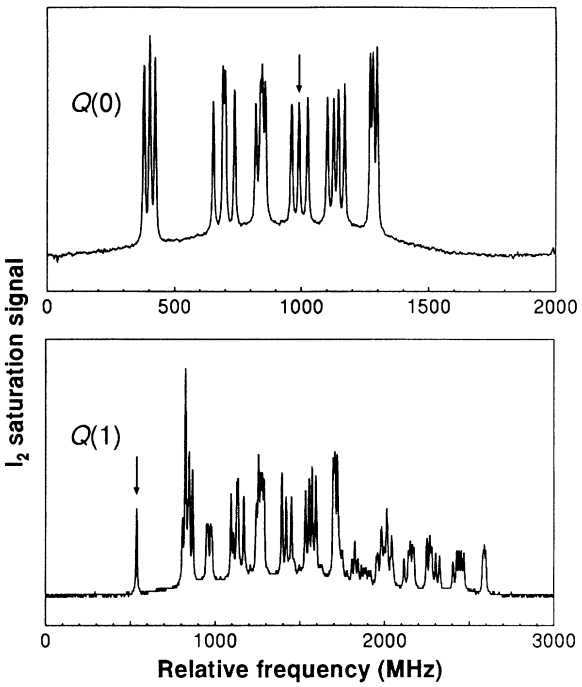

FIG. 8. Same as Fig. 5, for I_2 line 3417, used for $Q(0)$ branch in HD, and I_2 line 3374, used for $Q(1)$ branch.

varied significantly from one transition to another. The worst cases were the $60p$, $67p$, and $70p$ states, which had so many overlapping satellite lines that it was impossible to determine the line centers accurately. In five other cases, for the $71p$, $76p$, $78p$, $79p$, and $80p$ states, the satellites did not overlap the main transition and it was possible to determine the p state line centers to a few thousandths of a wave number. The three highest-n states that we observed are a special case. Transitions to each of the 78–80p states have large satellites partially overlapping the main transition (see Fig. 13). However, only one scan over these transitions was recorded, so it is not known if the relative size of the satellite lines would diminish with an attenuated probe laser. Fortunately, we could determine which peak is the actual np state by using predicted transition energies calculated from a MQDT fit to the observed $n=40-58$ states.

We suspect that the satellite lines are transitions to Rydberg states with $l\neq 1$. Dipole selection rules strongly favor transitions from the EF state to access p states, but Stark mixing in even a very weak stray electric field can lift this rule, as can the partial breakdown of gerade-ungerade symmetry in the heteronuclear HD molecule. Rydberg states with $l\geq 3$ have little core penetration and their quantum defects are near zero, so mixing with these

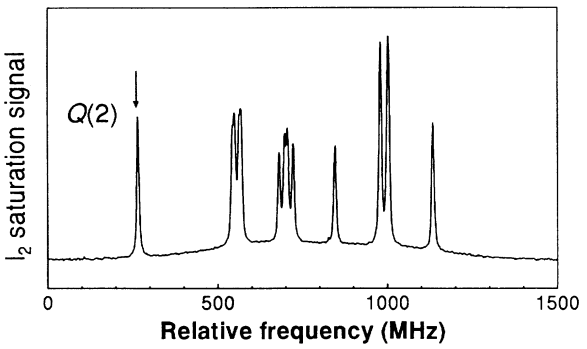

FIG. 7. Same as Fig. 5, for I_2 line 3515, used for $Q(2)$ branch in D_2.

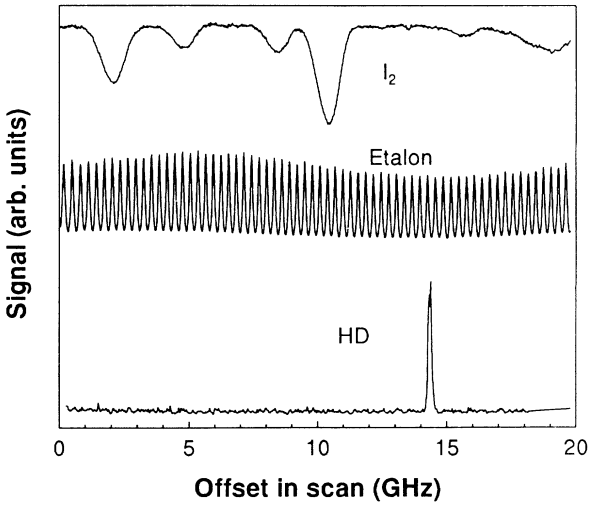

FIG. 9. The $R(0)$ branch of $41p\leftarrow EF$ in HD. Bottom: HD signal. Middle: marker étalon fringes. Top: I_2 absorption spectrum.

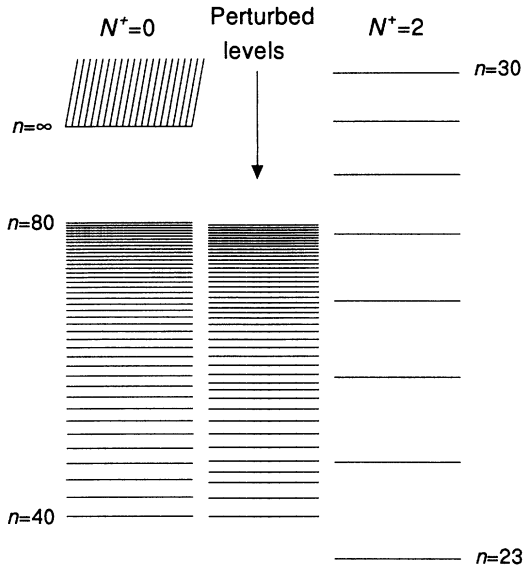

FIG. 10. Unperturbed Rydberg series converging to $N^+=0$ and 2 (left and right) and the perturbed Rydberg series resulting from the interaction of the two (center).

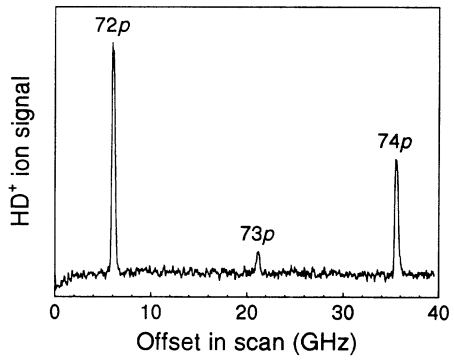

FIG. 11. Transitions to the 72p, 73p, and 74p states of HD showing a dramatic alteration in intensity due to interactions with the 27p state from the $N^+=2$ series.

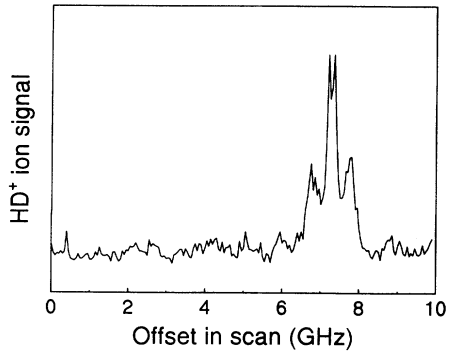

FIG. 12. Transition to the 60p state of HD, showing "satellite" lines.

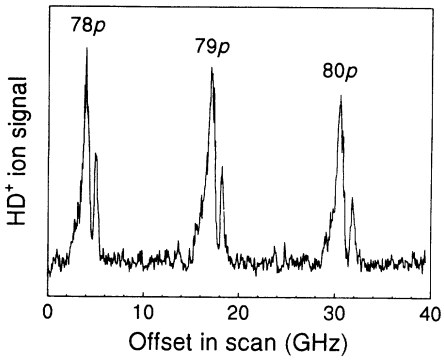

FIG. 13. Transitions to the 78p, 79p, and 80p states. The consistent "satellite" line pattern is unique to these three transitions. The larger, slightly asymmetric peaks are the main transitions.

states is expected to be strongest for np states whose quantum defects are near zero. No such pattern was observed, so the mixing must be with ns and nd states, whose quantum defects vary considerably. Unfortunately it is not possible to accurately estimate either the degree of Stark mixing with ns and nd states or the energies of transitions to these states without a detailed treatment of s-d mixing, which is beyond the scope of this work.

To test for the presence of stray electric fields a small dc voltage was intentionally applied between the field plates. With a field of 50 mV/cm pronounced changes were observed in the spectra. Reversing the polarity had no observable effect, setting an upper limit of 50 mV/cm on stray fields. In general, as the applied field was increased, additional lines appeared in the spectrum prior to the onset of measurable Stark shifting. In the 55p transition a field of 50 mV/cm induced additional lines, and at 250 mV/cm the original rather clean line was beginning to disappear in a blur of overlapped lines. However, the main line was shifted by less than the 0.004 cm^{-1} variation of the line-center measurements from one scan to another. Without the field and its concomitant extra lines, the line center was reproducible to within 0.001 cm^{-1} from scan to scan. Another test for Stark shifts was performed in the data analysis and will be discussed in Sec. V.

Another possible explanation for the satellite lines is that they are due to hyperfine splitting of the Rydberg states. However, the dramatic variation in the spacing, intensity, and number of the satellite lines from one principal quantum number to another is inconsistent with this hypothesis. Moreover, to the extent that the states we observe are singlets, there is no hyperfine structure [32]. We expect hyperfine structure to arise in the singlet Rydberg states from singlet-triplet mixing at high n, ultimately approaching the HD^+ hyperfine structure. This picture leads us to expect that hyperfine structure of the singlet states should be negligible until the electron exchange interaction (which falls off as n^{-3}) is comparable to the hyperfine splitting of the ion. This happens at $n \approx 99$, so the hyperfine structure should be negligible for the states observed in this work.

A detailed theoretical treatment of singlet-triplet mixing and the interaction of fine and hyperfine structure is beyond the scope of this work, but a study by Vassen and Hogervorst of singlet *np* states of atomic ^{3}He confirms that there is no significant singlet-triplet mixing until the electron exchange interaction is comparable to the hyperfine splitting [33].

V. ANALYSIS OF HD RYDBERG STATES

A. Extrapolation to the IP

We determine the ionization potential of HD using multichannel quantum-defect theory, whose parameters we fit to the measured energies of the *np* Rydberg states. The *np* Rydberg states have an angular momentum coupling intermediate between Hund's cases (b) and (d). Deviations from pure case-(d) coupling give rise to interactions between Rydberg series converging to different rotational levels of the molecular ion. These interactions manifest themselves by perturbing both the energy levels and transition strengths.

It is easiest to start with a case-(d) basis, corresponding to a nearly hydrogenic *np* Rydberg electron orbiting a HD^+ ion core in rotational level N^+. The total angular momentum excluding spins is specified by N, and in the absence of interactions all of the N sublevels are degenerate for each value of N^+. In this basis the energy of an *np* state relative to the $N^+=0$ ionization potential can be written as

$$E = E_{N^+} - \frac{\mathcal{R}_{\mathrm{HD}}}{(n-\delta_{N^+})^2} \ . \tag{1}$$

Here E_{N^+} is the rotational energy of the HD^+ ion in level N^+, and $\mathcal{R}_{\mathrm{HD}}$ is the reduced-mass Rydberg constant. The quantum defect δ_{N^+} is selected to match the observed energy, and is denoted with the subscript N^+ because it would be independent of n and N for an unper-

TABLE V. Transition energies and case-(d) quantum defects for $EF \leftarrow X$ transitions in HD.

			Transition energy		
n	δ_0	δ_2	(obs.)	(calc.)	(obs.)−(calc.)
40	0.0060	0.5731	25 198.5470	25 198.5478	−0.0008
41	0.0502	0.3854	25 201.7120	25 201.7071	0.0049
42	0.1667	0.2196	25 204.4462	25 204.4410	0.0052
43	0.8692	0.9886	25 208.1618	25 208.1675	−0.0057
44	0.9490	0.8333	25 210.6000	25 210.6001	−0.0001
45	0.9864	0.6779	25 212.9924	25 212.9944	−0.0020
46	0.0144	0.5280	25 215.2574	25 215.2562	0.0012
47	0.0532	0.3864	25 217.3602	25 217.3636	−0.0034
48	0.1251	0.2554	25 219.2716	25 219.2712	0.0004
50	0.8854	0.9615	25 223.4546	25 223.4476	0.0070
51	0.9438	0.8465	25 225.0512	25 225.0495	0.0017
52	0.9702	0.7325	25 226.6116	25 226.6053	0.0063
53	0.9922	0.6229	25 228.0934	25 228.0876	0.0058
54	0.0136	0.5177	25 229.4962	25 229.4914	0.0048
55	0.0396	0.4174	25 230.8186	25 230.8159	0.0027
56	0.0796	0.3226	25 232.0550	25 232.0569	−0.0019
57	0.1501	0.2343	25 233.1930	25 233.1946	−0.0016
58	0.3253	0.1589	25 234.1570	25 234.1606	−0.0036
61	0.9336	0.8741	25 237.7192	25 237.7176	0.0016
62	0.9569	0.7995	25 238.6398	25 238.6377	0.0039
63	0.9714	0.7263	25 239.5226	25 239.5189	0.0037
64	0.9823	0.6560	25 240.3694	25 240.3632	0.0062
65	0.9974	0.5887	25 241.1746	25 241.1703	0.0043
66	0.0090	0.5236	25 241.9466	25 241.9414	0.0052
67	0.0311	0.4616	25 242.6770	25 242.6779	−0.0009
68	0.0539	0.4019	25 243.3756	25 243.3808	−0.0052
69	0.0656	0.3437	25 244.0522	25 244.0507	0.0015
71	0.1497	0.2367	25 245.2840	25 245.2864	−0.0024
72	0.2354	0.1883	25 245.8374	25 245.8403	−0.0029
73	0.3875	0.1447	25 246.3320	25 246.3352	−0.0032
75	0.9280	0.0255	25 247.6732	25 247.7250	−0.0518
76	0.8413	0.9761	25 248.2248	25 248.2071	0.0177
77	0.8688	0.9333	25 248.6988	25 248.6805	0.0183
78	0.9401	0.8938	25 249.1350	25 249.1408	−0.0058
79	0.9510	0.8531	25 249.5828	25 249.5864	−0.0036
80	0.9630	0.8137	25 250.0136	25 250.0171	−0.0035

TABLE VI. Series limit of $np \leftarrow EF$ transitions and case-(b) quantum defects for HD, from MQDT fit.

Series limit	δ_σ	δ_π
25 267.141(11)	0.2012	−0.0832

turbed case-(d) Rydberg series.

The interactions between different Rydberg series obey the selection rule $\Delta N^+ = \pm 2$ for the homonuclear isotopomers. In the heteronuclear HD isotopomer, $\Delta N^+ = \pm 1$ interactions are also allowed but are expected to be very weak except near the dissociation thresholds [34]. We have found that in nearly all cases, a model incorporating only the $\Delta N^+ = \pm 2$ interactions accounts for the observed energy levels within experimental error. Figure 10 shows the $N = 1$ Rydberg states converging to the ion core levels $N^+ = 0$ and 2, illustrating the effects of the strong mixing between these two case-(d) Rydberg sequences.

Multichannel quantum-defect theory provides a simple description of coupled Rydberg series in terms of a few parameters, which are easily fitted to experimental results and can also sometimes be determined *ab initio* [35]. The key idea, described in Ref. [36], is to connect the case-(d) quantum defects defined in Eq. (1) with the case-(b) quantum defects δ_σ and δ_π that characterize the interaction of the Rydberg electron and the ion core at short range. The parameters of the model include these case-(b) quantum defects and the rotational energy levels E_{N^+} of the molecular ion core.

A two-channel model of the $N = 1$ Rydberg series in HD converging to $N^+ = 0$ and 2 relates the eigenenergies to the parameters with two conditions. The consistency condition requires that both case-(d) quantum defects must be consistent with Eq. (1):

$$E = -\frac{\mathcal{R}_{\rm HD}}{(n_0 - \delta_0)^2} = E_2 - \frac{\mathcal{R}_{\rm HD}}{(n_2 - \delta_2)^2} \ . \tag{2}$$

The electronic wave function must satisfy a boundary-value condition that requires

$$\begin{vmatrix} \sqrt{1/3}\sin\pi(\delta_0 - \delta_\Sigma) & \sqrt{2/3}\sin\pi(\delta_0 - \delta_\Pi) \\ -\sqrt{2/3}\sin\pi(\delta_2 - \delta_\Sigma) & \sqrt{1/3}\sin\pi(\delta_2 - \delta_\Pi) \end{vmatrix} = 0 \ .$$

These equations determine the case-(d) quantum defects, and consequently the energy levels, of all the $N = 1$ states from three parameters: E_2, δ_Σ, and δ_Π.

The energies predicted by Eqs. (2) and (3) are relative to the $N^+ = 0$ ionization potential. Comparison with the experimental energy levels, which are measured relative to the ground state, requires a fourth parameter: the ionization potential. These four parameters are fit to the measured energies with a computer program using the Marquardt-Levenberg least-squares algorithm [37,38]. The values for the series limit and case-(b) quantum defects converge quickly and are insensitive to the initial guesses for the parameters. However, the $N^+ = 2$ rotational energy E_2 converges more slowly and with a larger statistical error, suggesting that its value does not strongly influence the energies. Moreover, fixing the rotational interval at several different values near the *ab initio* value did not significantly affect the values to which the other parameters converged. Because of this, we determined the series limit and the case-(b) quantum defects with the rotational interval fixed at the *ab initio* value.

The fit included 35 transitions, excluding those that could not be measured accurately, and also the $74p$ transition because the root-finding algorithm was confused by a nearby level in the $N^+ = 2$ series. When the parameters determined by the fit were supplied to another program that calculated the eigenenergies using a different algorithm that did not suffer from this confusion, it predicted the $74p$ transition at 25 246.786 $\rm cm^{-1}$, only 0.004 $\rm cm^{-1}$ away from the measured value. Table V compares the observed transitions with the predictions of the MQDT model, using the parameters listed in Table VI.

The region spanned by this data contains four lines from the $N^+ = 2$ series. In the unperturbed series, the $24p_2$ state falls between the $43p_0$ and $44p_0$ states, the $25p_2$ state falls between the $49p_0$ and $50p_0$ states, the $26p_2$ state falls between the $59p_0$ and $60p_0$ states, and the $27p_2$ state falls between the $73p_0$ and $74p_0$ states. These np_2 states were not observed and a calculation of oscillator strengths indicated that transitions to these states are more than an order of magnitude weaker than to the neighboring np_0 states. The calculation also indicated that transitions to the $49p_0$, $58p_0$, and $73p_0$ states would have smaller oscillator strengths than neighboring transitions. In the experiment, the $49p$ transition was not observed despite scanning over the entire interval between $48p$ and $50p$. The $58p$ and $60p$ lines were quite strong, but the $59p$ transition was not seen at all. And as Fig. 11 shows, while the $73p$ transition was clearly observed, it is significantly weaker than the $72p$ and $74p$ lines in the same continuous laser scan.

Twelve transitions to $N^+ = 1$ states lie in the region studied. The data suggest that there may be some interactions between the two series, especially near $42p_1$,

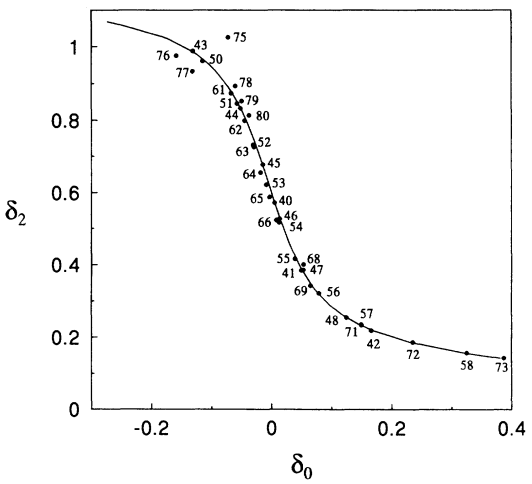

FIG. 14. Lu-Fano plot of the case-(d) quantum defects of the np Rydberg series in HD. The circles correspond to the observed transitions. The solid line represents a calculation using as input the three MQDT parameters fit to the data.

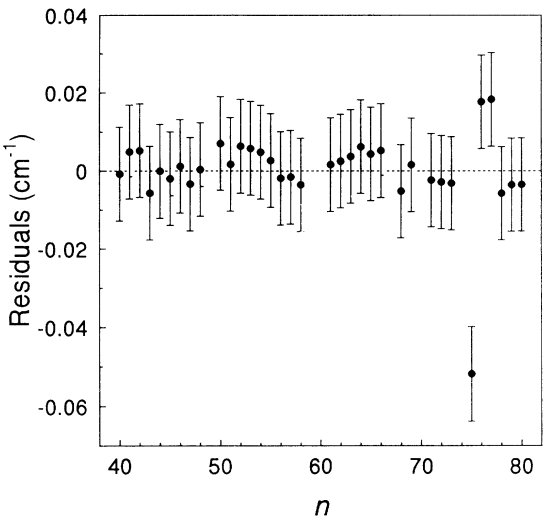

FIG. 15. Fit residuals of $np \leftarrow EF$ transitions.

which lies between $77p_0$ and $78p_0$, but nowhere else is there any effect that can be clearly distinguished from random scatter.

The quantum-defect fit gives a series limit of 25 267.141 cm^{-1}. The statistical uncertainty of the fit is 0.004 cm^{-1}. Other sources of error are discussed below and combine to give an uncertainty of 0.011 cm^{-1}. Figures 14 and 15 compare the observed transition energies and the quantum-defect model in the form of a Lu-Fano plot and a plot of fit residuals.

B. Sources of error

A constant impediment to precise spectroscopy of high-n Rydberg states is the Stark effect. As a starting point for considering possible Stark shifts in our data, we use as a model the Rydberg states of atomic helium. The overall trends will be the same in both of these two-electron systems, although individual levels in the H_2 isotopomers can behave somewhat erratically because of the large local changes in quantum defects caused by multichannel interactions. For $n \gg l$, low-field Stark shifts in helium scale as n^7. One test for Stark shifts is to fit quantum-defect parameters to subsets of the data and see how consistent the results are. This test shows no statistically significant variations. To evaluate the sensitivity of the test, a synthetic Stark shift $\Delta E_n = S(N/80)^7$ was computed and added to the measured transitions, then the MQDT fit was repeated. For $S = 0.02$ cm^{-1} the series limit found from the complete data set shifts by 0.0114 cm^{-1}, and fits to the subsets $n = 40$–58 and 61–80 differ by 0.0115 cm^{-1} compared to 0.0014 cm^{-1} for fits to the real data. For $S = 0.01$ cm^{-1}, the series limit shifts by 0.0056 cm^{-1} and fits to the subsets differ by 0.0051 cm^{-1}. The shift of the series limit should scale almost linearly with the difference between the two subsets, since the binding energy of the $80p$ state is three times smaller than the interval from $40p$ to $80p$. This indicates that the 0.0014 cm^{-1} difference between fits to the two subsets of the real data corresponds to a possible 0.0014-cm^{-1} shift of the ionization potential. Fits to smaller subsets were also performed, but statistical uncertainties were too large for these fits to be useful.

TABLE VII. Error budget for the series limit of the $np \leftarrow EF$ transitions.

I_2 atlas calibration	0.010
Quantum-defect fit	0.004
Doppler shifts	0.0017
Stark shifts	0.0014
Laser amplifier shift	0.0005
Boxcar time constant	0.0002
Uncertainties of individual line positions	0.0009
rms total	0.011

Table VII enumerates the various contributions to the uncertainty of the series limit of the $np \leftarrow EF$ transitions. The sources of error are essentially the same as for the $EF \leftarrow X$ transitions, but most are reduced in size since the transitions involve two photons at the fundamental cw laser wavelength, rather than six. As with the $EF \leftarrow X$ transitions, the uncertainty is dominated by the uncertainty in the overall calibration of the iodine atlas. The laser amplifier shift for LDS-751 laser dye near 794 nm was previously measured to be 8±8 MHz [1], or 0.0005 cm^{-1} in the $np \leftarrow EF$ transitions. As we did for the $EF \leftarrow X$ transitions, we take twice the measured shift as the uncertainty. The errors due to uncertainties of the iodine lines within the atlas (≈ 0.003 cm^{-1}), scan linearization (≈ 0.003 cm^{-1}), finding the centers of the iodine lines (≈ 0.002 cm^{-1}), data granularity (0.0017 cm^{-1}), and étalon free spectral range (≈ 0.0003 cm^{-1}) are uncorrelated from one transition to another, so their contribution to the uncertainty in the series limit is reduced by the square root of the number of degrees of freedom, to 0.0009 cm^{-1}. This is not the case for errors due to the uncertainty in the overall calibration of the iodine atlas (0.010 cm^{-1}), the statistical uncertainty of the fit (0.004 cm^{-1}), Stark shifts (0.0014 cm^{-1}), laser amplifier shift (estimated to be 0.0005 cm^{-1}), shifts due to the boxcar-averager (≈ 0.0002 cm^{-1}), and Doppler shifts due to misalignment of the lasers (0.0017 cm^{-1}). These sources of error are not correlated with one another, so we add them in quadrature to obtain the 0.011 cm^{-1} uncertainty of the series limit.

VI. RESULTS FOR THE IONIZATION POTENTIALS

The ionization potential of HD is obtained from the series limit of the $np \leftarrow EF$ transitions by adding the term energy of the ($N = 0$, $v = 0$) level of the EF state, 99 301.338(17) cm^{-1}. This gives a value of 124 568.479(20) cm^{-1} for the ionization potential, where the uncertainty is the quadrature sum of the uncertainties of the series limit and the EF-state uncertainty. Preliminary results from the calibration of the iodine reference lines for the high-resolution data by Shiner and coworkers [18] indicate that the IP value will change very little, although the uncertainty will be reduced slightly. The result agrees very well with the theoretical value of 124 568.486 cm^{-1} [4,7,39].

The best previous measurement was by Takezawa and

Tanaka, who measured Rydberg *np* states up to $n=40$ using direct VUV excitation from the ground state [40]. They originally published a value of 124 569.5(6) cm^{-1}, but Herzberg and Jungen pointed out that this should be corrected by a pressure shift of 1.05 cm^{-1} [36,41]. With this correction, the value is 124 568.4(6), in good agreement with the value reported here but less accurate by a factor of 30.

For the H_2 isotope the new *EF*-state measurements slightly alter the IP values reported in Refs. [1] and [2]. Our earlier result is lowered by 0.017 cm^{-1}, to 124 417.507(18) cm^{-1} [1]. Very little further change is expected when the high-resolution *EF*-state calibration is used instead, except that the uncertainty will be reduced to 0.012 cm^{-1}. The IP value given in Ref. [2] should be lowered by a similar amount, since it also relied on our earlier *EF*-state measurements. The agreement with the theoretical value of 124 417.512 cm^{-1} remains very close.

For D_2, a new value of the IP has very recently been obtained by Herzberg and co-workers, by combining the results reported here with new measurements of numerous low-*n*, high-*l* Rydberg states. Their result of 124 745.353(24) cm^{-1} is presented in a separate publication [3]. It differs only slightly from the current theoretical value of 124 745.382 cm^{-1}.

Taken together, these results for H_2, D_2, and HD provide a very stringent test of *ab initio* calculations, including the relativistic and radiative corrections. For H_2, the relativistic correction to the IP is 1.02 cm^{-1} and the radiative correction is 0.378 cm^{-1}, and the other isotopomers have corrections of similar size [7,15,42]. Thus these small but fundamental effects can presently be tested at the 2–5 % level, with further improvements expected.

VII. CONCLUSIONS

The *EF*-state term energies reported here establish a new overall calibration of the excited-state energy levels of H_2, D_2, and HD. Now accurate to 0.015 cm^{-1}, these results will be further improved to 0.003 cm^{-1} by recently completed measurements of the iodine hyperfine lines used as references [18]. Apart from this reference line calibration, the error budget is dominated almost completely by a single effect, the laser frequency shifts and chirping caused by the pulsed laser amplifier. We are confident that measurements of these VUV intervals to 0.001 cm^{-1} will be easily attainable by measuring the frequency and phase of the laser pulse, a process that can be accomplished by beating the output of the pulsed amplifier against a frequency-shifted sample of its cw input.

Our result for the ionization potential of HD continues the remarkable overall agreement found in recent experimental and theoretical work on the other isotopic variants of molecular hydrogen. The *np* state spectra also confirm the very nearly homonuclear character of the electronic structure of HD, which has been noted previously [43,34]. Only in one instance do we observe a noticeable breakdown of the two-channel MQDT model, although the presence of several "satellite" lines near the *np* states suggests that weak *l* mixing may be occurring in several cases. This additional structure should be an interesting object for future observations, but does not seriously compromise the IP determination.

No serious constraints appear to impede further improvement of the IP values for H_2, D_2, and HD to an accuracy of about 0.001 cm^{-1}, or even slightly better. At this level not only will the $EF \leftarrow X$ measurements become very difficult, but small perturbations of the Rydberg states are likely to introduce significant errors. Still, such a measurement will be a formidable challenge for molecular theory, and a very stringent test of QED effects in two-center systems.

ACKNOWLEDGMENTS

We wish to thank Gerhard Herzberg and David Shiner for numerous communications, and for providing results prior to publication. This research was supported by the National Science Foundation, Grants No. PHY-9000375 and No. PHY-9019524, and by a Precision Measurement Grant from the National Institute of Standards and Technology.

*Present address: Time and Frequency Division, National Institute of Standards and Technology, Boulder, CO 80303.

[1] E. McCormack, J. M. Gilligan, C. Cornaggia, and E. E. Eyler, Phys. Rev. A **39**, 2260 (1989).
[2] C. Jungen, I. Dabrowski, G. Herzberg, and M. Vervloet, J. Chem. Phys. **93**, 2289 (1990).
[3] C. Jungen, I. Dabrowski, G. Herzberg, and M. Vervloet, J. Mol. Spectrosc. (to be published).
[4] W. Kołos, K. Szalewicz, and H. J. Monkhorst, J. Chem. Phys. **64**, 3273 (1986).
[5] L. Wolniewicz and T. Orlikowski, Mol. Phys. **74**, 103 (1991).
[6] R. Bukowski, B. Jeziorski, R. Moszyński, and W. Kolos (unpublished).
[7] G. G. Balint-Kurti, R. E. Moss, I. A. Sadler, and M. Shapiro, Phys. Rev. A **41**, 4913 (1990).
[8] R. E. Moss, Chem. Phys. Lett. **172**, 458 (1991).
[9] E. E. Eyler, Comments At. Mod. Phys. **24**, 299 (1990).
[10] W. L. Glab and J. P. Hessler, Phys. Rev. A **35**, 2102 (1987).
[11] D. W. Chandler and L. R. Thorne, J. Chem. Phys. **85**, 1733 (1986).
[12] D. M. Bishop and L. M. Cheung, J. Phys. B **11**, 3133 (1978).
[13] D. M. Bishop and L. M. Cheung, Adv. Quantum Chem. **12**, 1 (1980).
[14] D. M. Bishop and L. M. Cheung, J. Chem. Phys. **75**, 3155 (1981).
[15] D. M. Bishop and L. M. Cheung, J. Chem. Phys. **69**, 1881 (1978).
[16] A. Dalgarno and A. E. Kingston, Proc. R. Soc. London, Ser. A **259**, 424 (1960).
[17] J. D. Garcia, Phys. Rev. **147**, 66 (1966).

[18] D. Shiner, W. Lichten, and J. M. Gilligan (unpublished).
[19] W. L. Glab and J. P. Hessler, Appl. Opt. **26**, 3181 (1987).
[20] S. Gerstenkorn and P. Luc, *Atlas du Spectre d'Absorption de la Molécule de l'Iode entre 14 800 et 20 000 cm^{-1}* (CNRS, Paris, 1978).
[21] S. Gerstenkorn and P. Luc, *Atlas du Spectre d'Absorption de la Molécule de l'Iode (14 800 cm^{-1}–15 600 cm^{-1})* (Laboratoire Aimé Cotton, Orsay, 1978).
[22] S. Gerstenkorn, J. Verges, and J. Chevillard, *Atlas du Spectre d'Absorption de la Molécule de l'Iode (11 000 cm^{-1}–14 000 cm^{-1})* (Laboratoire Aimé Cotton, Orsay, 1982).
[23] S. Gerstenkorn and P. Luc, Rev. Phys. Appl. (Paris) **14**, 791 (1979).
[24] J. M. Gilligan, Ph.D. thesis, Yale University, 1991.
[25] R. P. Hackel and S. Ezekiel, Phys. Rev. Lett. **42**, 1736 (1979).
[26] C. J. Bordé, G. Camy, B. Decomps, and J.-P. Descoubes, J. Phys. (Paris) **42**, 1393 (1981).
[27] J. P. Hessler and W. L. Glab (unpublished).
[28] M. S. Fee, K. Danzmann, and S. Chu, Phys. Rev. A **45**, 4911 (1992).
[29] E. E. Eyler, J. Gilligan, E. McCormack, A. Nussenzweig, and E. Pollack, Phys. Rev. A **36**, 3486 (1987).
[30] C. Schwartz and R. J. Le Roy, J. Mol. Spectrosc. **121**, 420 (1987).
[31] E. F. McCormack, Ph.D. thesis, Yale University, 1989.
[32] G. B. Field, W. B. Somerville, and K. Dressler, Annu. Rev. Astron. Astrophys. **4**, 207 (1966).
[33] W. Vassen and W. Hogervorst, Phys. Rev. A **39**, 4615 (1989).
[34] N. Y. Du and C. H. Greene, J. Chem. Phys. **85**, 5430 (1986).
[35] S. Ross and C. Jungen, Phys. Rev. Lett. **59**, 1297 (1987).
[36] G. Herzberg and C. Jungen, J. Mol. Spectrosc. **41**, 425 (1972).
[37] P. R. Bevington, *Data Reduction and Error Analysis for the Physical Sciences* (McGraw-Hill, New York, 1969), Chap. 11.
[38] W. H. Press, B. P. Flannery, S. A. Teukolsky, and W. T. Vetterling, *Numerical Recipes* (Cambridge, New York, 1986), Chap. 14.
[39] G. W. Erickson, J. Phys. Chem. Ref. Data **6**, 831 (1977).
[40] S. Takezawa and Y. Tanaka, J. Chem. Phys. **56**, 6125 (1972).
[41] S. Takezawa, J. Mol. Spectrosc. **54**, 379 (1975).
[42] D. M. Bishop and L. M. Cheung, Chem. Phys. Lett. **55**, 593 (1978), and erratum, Ref. [44].
[43] I. Dabrowski and G. Herzberg, Can. J. Phys. **54**, 525 (1976).
[44] D. M. Bishop and L. M. Cheung, Chem. Phys. Lett. **58**, 320(E) (1978).
[45] M. D. Levenson and A. L. Schawlow, Phys. Rev. A **6**, 10 (1972).